

# Chalcogen Bonding: Experimental and Theoretical Determinations from Electron Density Analysis. Geometrical Preferences Driven by Electrophilic–Nucleophilic Interactions

Mariya E. Brezgunova,<sup>†</sup> Julien Lieffrig,<sup>‡</sup> Emmanuel Aubert,<sup>†</sup> Slimane Dahaoui,<sup>†</sup> Pierre Fertey,<sup>§</sup> Sébastien Lebègue,<sup>†</sup> János G. Ángyán,<sup>†</sup> Marc Fourmigué,<sup>‡</sup> and Enrique Espinosa\*,<sup>†</sup>

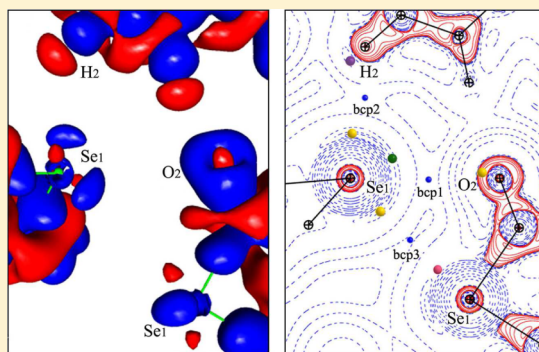
<sup>†</sup>CRM<sup>2</sup>, UMR 7036, Institut Jean Barriol, Lorraine University and CNRS, BP 70239, 54506 Vandoeuvre-lès-Nancy, France

<sup>‡</sup>Institut des Sciences Chimiques de Rennes, Université Rennes 1 UMR CNRS 6226, Campus de Beaulieu, 35042 Rennes, France

<sup>§</sup>Synchrotron Soleil, L'Orme des Merisiers Saint-Aubin, BP 48, 91192 Gif-sur-Yvette, France

## S Supporting Information

**ABSTRACT:** Chalcogen bonding has been investigated in terms of the electron density distribution  $\rho(\mathbf{r})$  around chalcogen atoms. The evolution of  $\rho(\mathbf{r})$  along the series of chalcogen atoms is shown based on ab initio calculations on chalcogenophthalic anhydrides  $C_8O_2H_4\text{Chal}$  (Chal = O, S, Se, and Te), where the Chal atom is in its  $sp^3$  hybridization. From a detailed analysis of the experimental and theoretical electron density and the  $L(\mathbf{r}) = -\nabla^2\rho(\mathbf{r})$  function in the crystal phase of  $C_8O_2H_4\text{Se}$ , we characterize directionality and strength of chalcogen bonding (Se $\cdots$ O and Se $\cdots$ Se) and hydrogen bonding (Se $\cdots$ H) interactions. In addition, several isolated dimers and a trimer of  $C_8O_2H_4\text{Se}$  have been also studied at the X-ray geometry in order to compare interaction energies with those estimated from the measured electron density. Similarly to halogen atoms in halogen bonding interactions, the anisotropic distribution of  $\rho(\mathbf{r})$  around the Chal atoms was found to be at the origin of chalcogen bonding. Therefore, the concepts, developed earlier for halogen bonding, are extended here to chalcogen bonding interactions. From the results of this work, the  $L(\mathbf{r})$  function proves to be more precise than the  $\sigma$ -hole concept to identify electrophilic sites of Se-atoms in  $sp^3$  hybridization.



The understanding and the control of intermolecular interactions play a crucial role in molecular recognition, crystal engineering, and biological systems.<sup>1</sup> While conventional hydrogen bonding (e.g.,  $\text{NH}\cdots\text{O}$  and  $\text{OH}\cdots\text{O}$ ) has been acknowledged for a long time,<sup>2</sup> weaker interactions such as  $\text{CH}\cdots\text{O}$ ,<sup>3</sup>  $\text{CH}\cdots\pi$ ,<sup>4</sup> and halogen bonding<sup>5</sup> have been also recognized to stand out in supramolecular architectures.

Halogen bonding, first identified in  $\text{H}_3\text{N}\cdots\text{I}_2$ <sup>6</sup> and  $\text{Br}_2\cdots\text{Br}_2$ ,<sup>7</sup> was extensively characterized by Hassel,<sup>8</sup> Bent,<sup>9</sup> and others. Politzer, Murray, and Awwadi associated its origin with the presence of an electropositive region of the electrostatic potential<sup>10</sup> in the prolongation of the C–Hal bond (Hal = Cl, Br, and I), called  $\sigma$ -hole, that interacts with an electron-rich moiety of another Hal atom or a Lewis base (B) through an essentially electrostatic C–Hal $\cdots$ X, (X = B, Hal) interaction.<sup>11</sup> Strength and directionality of halogen bondings, particularly with the most polarizable iodine atom, activated by electron-withdrawing substituents (as in  $\text{F}_{2n+1}\text{C}_n\text{--I}$  and  $\text{C}_6\text{F}_{6-n}\text{I}_n$  or in iodoacetylenes), allowed its extensive use in crystal engineering<sup>12</sup> toward the elaboration of halogen-bonded supramolecular architectures. A recent experimental and theoretical charge density study involving  $\text{C}_6\text{Cl}_6$ <sup>13</sup> has demonstrated that the origin of the  $\sigma$ -hole concept is found in the anisotropic electron

density distribution  $\rho(\mathbf{r})$  around the Hal-nuclei, a feature called polar flattening. As a consequence of this anisotropy, electrophilic and nucleophilic regions, mostly perpendicularly placed to each other, can be simultaneously involved in highly directional Hal $\cdots$ Hal interactions. The directionality of the halogen bonds has been recently analyzed by A. Stone,<sup>14</sup> who found that the  $\sigma$ -hole concept mapped by the electrostatic potential cannot completely explain the preferred orientation, which is strongly influenced by overlap repulsion effects as well.

The  $\sigma$ -hole concept has been extended from halogens to divalently bonded group VI chalcogens<sup>10b</sup> to rationalize the frequent occurrence of S $\cdots$ O and S $\cdots$ S intra-<sup>15</sup> and intermolecular<sup>16</sup> interactions. Statistical analyses of crystal structures<sup>17</sup> and theoretical calculations<sup>18</sup> revealed their preferred conformations with Lewis bases pointing toward the chalcogen atom approximately along the extension of one of the two covalent bonds to the chalcogen atom. In theoretical gas phase studies, the prevalence of either electrostatic<sup>19</sup> or dispersion<sup>20</sup> contributions to the energetic stabilization of the

Received: May 3, 2013

Revised: June 22, 2013

Published: June 25, 2013

chalcogen bond is underlined, noting that polarization and charge transfer<sup>21</sup> are also not negligible, depending on the system. On the other hand, experimental investigations of chalcogen bonding interactions are very sparse and involve only light chalcogen atoms (O and S).<sup>22</sup> In these cases, the interaction has been mostly considered in terms of the Lewis acid–base concept; however, a deeper understanding of the force driving the specific orientations between the bonded molecules has never been attempted experimentally. For this reason, we have decided to undertake an electron density analysis of a series of chalcogenated molecules showing chalcogen bonding interactions in crystal phases. Looking for a model series, we concentrated our efforts on chalcogenophthalic anhydrides  $C_8O_2H_4\text{Chal}$  (hereafter, PA, TPA, SePA, and TePA with Chal = O, S, Se, and Te, respectively), where the two electron-withdrawing carbonyl groups are expected to enhance the  $\sigma$ -hole structure of the central chalcogen atom.

The reported X-ray crystal structures of the three compounds, TPA,<sup>24</sup> SePA,<sup>25</sup> and TePA<sup>25</sup>, show indeed a recurrent structural motif with  $\text{Chal}\cdots\text{O}=\text{C}$  angles ( $\chi$ ) that describe the geometry of the carbonyl group lone pair pointing toward the Chal atom (Table 1). Although the  $\text{Chal}\cdots\text{O}$

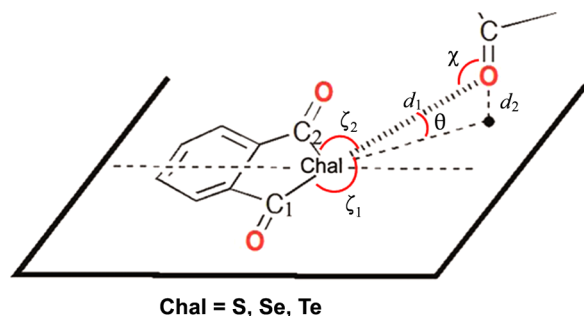
**Table 1. Crystal Structure Characteristics of Chalcogen Bonding for TPA, SePA, and TePA at Room Temperature (Chal = S, Se, and Te).<sup>a</sup>**

$\text{Chal}\cdots\text{O}$	$d_1$	$\omega$	$\zeta_1/\zeta_2$	$\chi$	$\theta$
$\text{S}\cdots\text{O}$	3.469	104.5	139.6/118.4	115.1	23.5
$\text{Se}\cdots\text{O}$	3.413	99.7	144.5/120.5	111.5	19.8
$\text{Te}\cdots\text{O}$	3.375	99.3	145.9/126.6	109.1	17.0

<sup>a</sup>Distance  $\text{Chal}\cdots\text{O}$  ( $d_1$  / Å), penetration parameter ( $\omega$  / %), defined as the  $\text{Chal}\cdots\text{O}$  distance over the sum of van der Waals radii,<sup>23</sup> and angles ( $^\circ$ ):  $\zeta_i = \text{Ci}-\text{Chal}\cdots\text{O}$  ( $i = 1, 2$ ),  $\chi = \text{Chal}\cdots\text{O}=\text{C}$ , and  $\theta = \arcsin(d_2/d_1)$  (see Scheme 1).

distances are not significantly shorter than the sum of the van der Waals radii (see the  $\omega$  parameter in Table 1), a strengthening seems to appear going down in the chalcogen series. Indeed, the diminution of the  $\omega$  value in conjunction with that of the  $\theta$  angle (Scheme 1) indicates a closer  $\text{Chal}\cdots\text{O}$

**Scheme 1. Geometrical Characterization of  $\text{Chal}\cdots\text{O}$  Interaction in TPA, SePA, and TePA**



disposition, while the oxygen atom is going into the basal plane of the chalcogenated molecule, favoring the interaction of the oxygen lone pair, with the expected electrophilic region ( $\sigma$ -hole) of the chalcogen atom. At the same time, the  $\text{C}_i-\text{Chal}\cdots\text{O}$  angles ( $\zeta_1$  and  $\zeta_2 \sim 120\text{--}140^\circ$ ) show that the electron-rich oxygen atom is not located in the prolongation of the  $\text{C}-\text{Chal}$  bonds, as anticipated from earlier models. These three examples

(TPA, SePA, and TePA) indicate that the electrostatic  $\sigma$ -hole concept does not totally explain all the geometrical cases of the underlined interaction, as recently pointed out for halogen bonds;<sup>14</sup> thereby, a more appropriate parameter should be introduced.

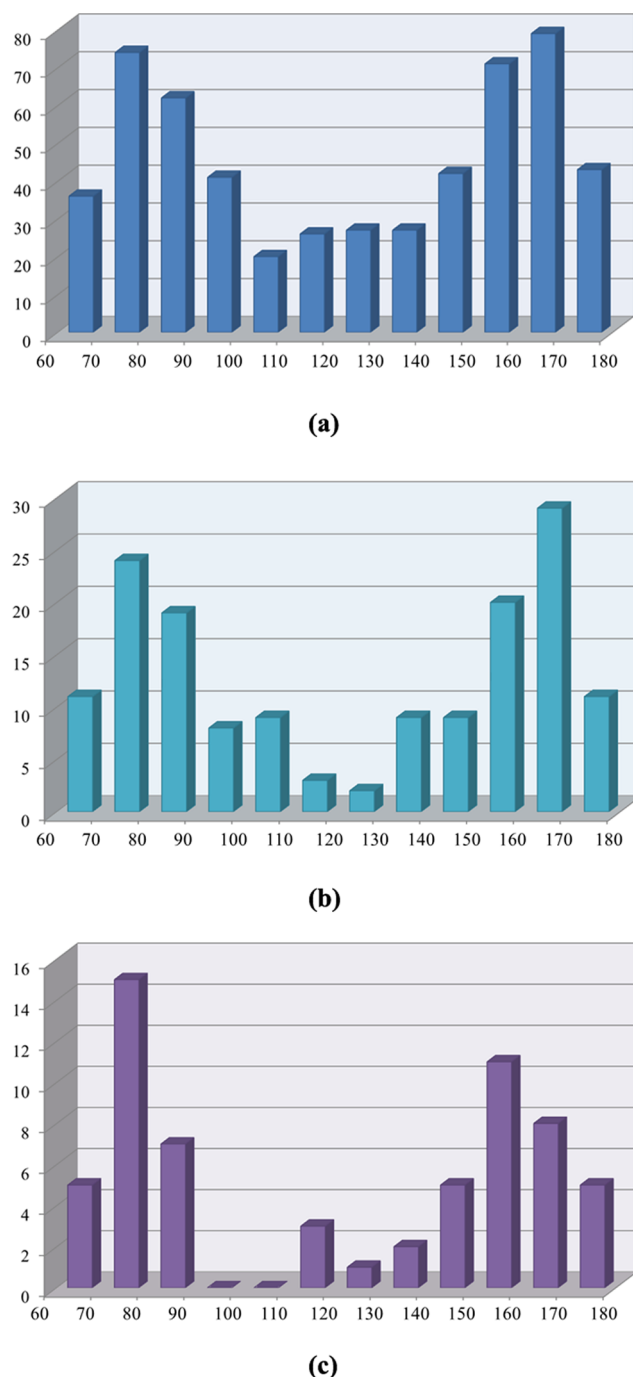
Indeed, the statistical analysis of the preferred orientation of the O atom in the carbonyl group with respect to both  $\text{C}_i-\text{Chal}$  bonds ( $i = 1, 2$ ; Chal = S, Se, and Te in  $sp^3$  hybridization) leads to the angular distributions  $\text{C}_1-\text{Chal}\cdots\text{O}$  ( $\zeta_1$ ) and  $\text{C}_2-\text{Chal}\cdots\text{O}$  ( $\zeta_2$ ) displayed in Figure 1 (see the Supporting Information for the conditions of the Cambridge Structural Database statistical study). Two peaks of angular distributions are approximately centered at  $\zeta_1 \approx 165^\circ$  and  $\zeta_2 \approx 75^\circ$  for both S and Se and at  $\zeta_1 \approx 155^\circ$  and  $\zeta_2 \approx 75^\circ$  for Te. In addition, a non-negligible number of contacts presenting  $\text{C}_i-\text{Chal}\cdots\text{O}$  angles from  $110$  to  $140^\circ$ , which corresponds to the position of the O atom roughly close to the prolongation of the bisecting  $\text{C}_1-\text{Chal}-\text{C}_2$  direction, also appear. While the former peaks indicate the position of the  $\sigma$ -hole approximately along the  $\text{C}-\text{Chal}$  bonds, and therefore reveal the preferred directions of nucleophilic attacks, data within the  $110\text{--}140^\circ$  range point toward the participation of other characteristic sites in the formation of chalcogen interactions, as demonstrated below.

Hereafter, we present a detailed analysis of the electron distribution in the series PA, TPA, SePA, and TePA. First, on the basis of ab initio calculations on isolated species, we show the evolution of electron distributions along the series of chalcogen atoms. Then, from a rigorous analysis of the accurate experimental and theoretical  $\rho(\mathbf{r})$  in the crystal phase of SePA, we determine the parameters describing the directionality and the strength of chalcogen bonding from  $\rho(\mathbf{r})$  properties observed in intermolecular regions. In addition, several isolated dimers and a trimer of SePA have been also studied at the X-ray geometry in order to compare interaction energies with those estimated from the measured electron density.

Selenophthalic anhydride (SePA) was prepared as previously described from phthaloyl chloride and  $\text{LiAlHSeH}$  in THF.<sup>27</sup> Single crystals of SePA were obtained by the sublimation method at  $50^\circ\text{C}$ . X-ray diffraction measurements were carried out using a Mo  $K\alpha$  radiation source ( $\lambda = 0.71073$  Å) on an Enraf-Nonius diffractometer with a Kappa-CCD detector up to a maximum resolution of  $(\sin \theta/\lambda)_{\text{max}} = 1.28$  Å<sup>-1</sup>,  $T = 100(4)$  K (Oxford Cryosystems  $\text{N}_2$  cooling device), with 226518 reflections collected. The crystal structure was determined in the monoclinic system,  $P2_1/n$  space group, and unit cell parameters of  $a = 8.3167(1)$  Å,  $b = 5.7518(1)$  Å,  $c = 15.1598(2)$  Å,  $\beta = 102.841(1)^\circ$ ,  $V = 707.05(2)$  Å<sup>3</sup>. Further experimental details are given in the Supporting Information.

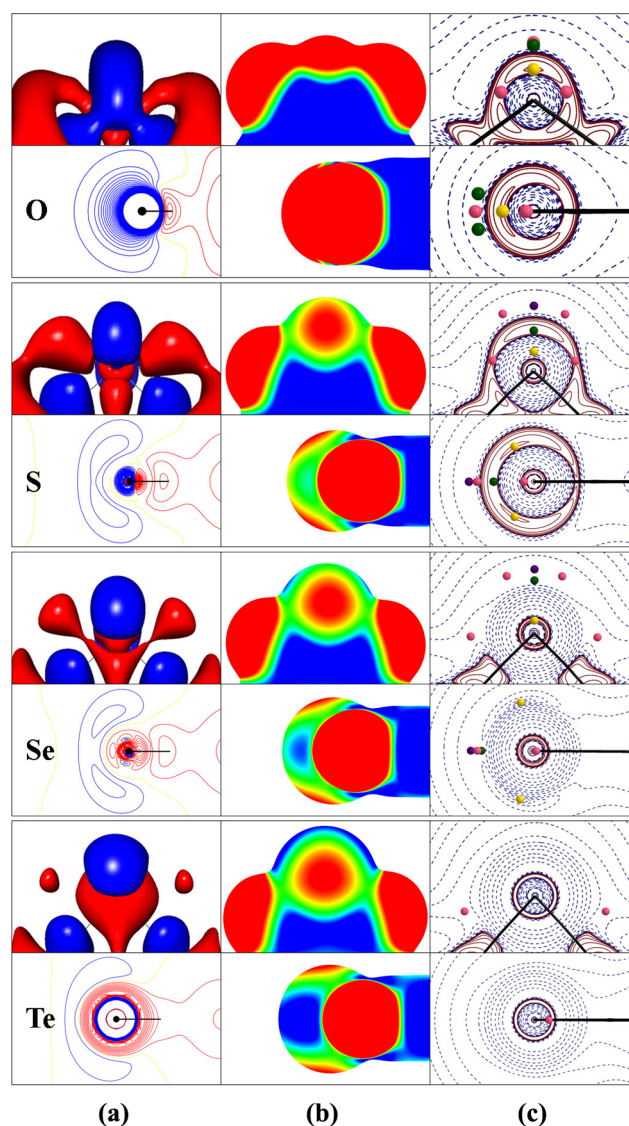
Ab initio periodic calculations using density functional theory have been performed on the crystal structure of SePA with the Vienna ab initio simulation package (VASP).<sup>28</sup> The experimental structure of SePA was used without any optimization of atomic positions or unit cell parameters. The all-electron frozen core PAW (Projector Augmented Wave) method was used with the PBE exchange-correlation functional.<sup>29</sup> Further information, as well as details of ab initio quantum chemical calculations on isolated monomers, dimers, and the trimer is given in the Supporting Information.

Figure 2 shows the electron density deformation  $\Delta\rho(\mathbf{r}) = \rho(\mathbf{r}) - \Sigma\rho_{\text{sph}}^{\text{at}}(\mathbf{r})$ , the electrostatic potential  $V(\mathbf{r})$ , and the  $L(\mathbf{r}) = -\nabla^2\rho(\mathbf{r})$  maps for  $C_8O_2H_4\text{Chal}$  (Chal = O, S, Se, and Te) monomers optimized in gas phase.  $\Delta\rho(\mathbf{r})$  characterizes the charge redistribution with respect to the superposition of



**Figure 1.** Number of data of C–Chal...O ( $\zeta$ /°) angular distributions (see Scheme 1), showing the preferred orientation of the O atom in the carbonyl group with respect to both  $C_i$ –Chal bonds (Chal = S, Se, and Te in  $sp^3$  hybridization): (a) Chal = S ( $N = 548$ ), (b) Chal = Se ( $N = 154$ ), (c) Chal = Te ( $N = 62$ ).  $N$  corresponds to the number of  $C_2\text{Chal}_{sp^3}\cdots\text{O}=\text{CX}_2$  fragments observed in the Cambridge Structural Database.<sup>26</sup> Only fragments holding the criteria:  $\alpha_{C-\text{Chal}-C} = 80\text{--}100^\circ$ ,  $\chi_{\text{Chal}\cdots\text{O}=\text{X}} = 90\text{--}130^\circ$ , and  $d_{\text{Chal}\cdots\text{O}} < r_{\text{vdw}}(\text{Chal}) + r_{\text{vdw}}(\text{O}) + 0.3 \text{ \AA}$  are included in the statistics.

spherically averaged noninteracting atomic densities, showing the formation of lone pairs and chemical bonds. The  $sp^3$  hybridization of chalcogen atoms is observed in the  $\Delta\rho(\mathbf{r})$  maps (Figure 2a), where the electron distribution associated to the lone pairs ( $\delta^-$  regions) is grouped in the plane bisecting the C–Chal–C angle. The progressive separation of the chalcogen



**Figure 2.** Maps around chalcogen atoms in  $C_8O_2H_4\text{Chal}$  monomers [(C–Chal–C plane (top) and the perpendicular plane bisecting the C–Chal–C angle (bottom)]: (a) Deformation density  $\Delta\rho(\mathbf{r})$  [iso-surfaces and contours are drawn at the  $\pm 0.05 \text{ e\AA}^{-3}$  levels: positive (blue) and negative (red)], (b) electrostatic potential  $V(\mathbf{r})$  ( $\text{e \AA}^{-1}$ ) displayed on the molecular  $\rho(\mathbf{r})$  iso-surface of 0.001 au [from the most positive (blue) to the most negative (red) values], and (c)  $L(\mathbf{r}) = -\nabla^2\rho(\mathbf{r})$  [ $\text{e\AA}^{-5}$ , contours are in logarithmic scale: positive (red) and negative (blue)]. Charge concentration and charge depletion (CC/CD) sites are marked in  $L(\mathbf{r})$  maps [CC: (3, -3) (yellow); CD: (3, -1) (green), (3, +1) (pink), and (3, +3) (violet)]. Monomers are calculated at the MP2/aug-cc-pVTZ level. Lone-pair (lp) directions are obtained from the  $\Delta\rho(\mathbf{r})$  maxima in the bottom figure of each atom in (a).

lone pairs (lp) along the series  $O < S < Se < Te$  ( $lp_1$ –nucleus– $lp_2 = 0, 114, 120$ , and  $130^\circ$ , Figure 2a bottom) follows the decrease of the C–Chal–C angle ( $109.9, 92.3, 88.2$ , and  $82.4^\circ$ , respectively) and is accompanied by more extended and less concentrated  $\delta^-$  regions. Simultaneously, electron deficient ( $\delta^+$ ) regions along the C–Chal directions are reduced and shifted toward the external part of the chalcogen atom through the series from S to Te atoms (Figure 2a, top). The positive and negative regions of the electrostatic potential  $V(\mathbf{r})$  on the molecular  $\rho(\mathbf{r})$  iso-surface of 0.001 au ( $0.0067 \text{ e\AA}^{-3}$ ) around



the chalcogen atoms (Figure 2b) follow the disposition and the intensity of the  $\delta^+$  and  $\delta^-$  regions found in the  $\Delta\rho(\mathbf{r})$  maps. Thus, along the C–Chal direction, the values of  $V(\mathbf{r})$  are 0.61, 1.66, and  $3.25 (\times 10^{-2} \text{ e } \text{\AA}^{-1})$  for S, Se, and Te, respectively, while at the lone-pairs position,  $V(\mathbf{r})$  is  $-7.52$ ,  $-2.10$ ,  $-2.15$ , and  $-2.15 (\times 10^{-2} \text{ e } \text{\AA}^{-1})$  for O, S, Se, and Te, respectively.

The  $L(\mathbf{r})$  function indicates the molecular regions where the charge density is locally concentrated ( $L(\mathbf{r}) > 0$ ) or depleted ( $L(\mathbf{r}) < 0$ ).  $\delta^+$  and  $\delta^-$  distributions arising from  $\Delta\rho(\mathbf{r})$  find their physical interpretations in the charge depletion (CD) and charge concentration (CC) regions of  $\rho(\mathbf{r})$ , which can be identified by the  $L(\mathbf{r})$  function. In accordance with the topological analysis of  $L(\mathbf{r})$  in the atomic valence shell charge concentration (VSCC) of light atoms,<sup>30</sup> such as O, F, S, and Cl, saddle and local maxima distributions permit the location of atomic electrophilic and nucleophilic sites from the observation of (3, +1) and (3, −3) critical points (CPs). For heavier atoms, such as Se, Br, Te, and I, the whole valence shell of the atom (including its charge depletion region, VSCD) is needed<sup>31</sup> and additional (3, +3) and (3, −1) CPs must be considered. Thereby, a (3, −3) CP of  $L(\mathbf{r})$  indicates a local maximum of electron density (CC region) along the three main directions, while (3, −1), (3, +1), and (3, +3) CPs correspond to a local minimum (CD region) along one, two, and three main directions. Paralleling the separation of the lone pairs observed in  $\Delta\rho(\mathbf{r})$  and  $V(\mathbf{r})$  maps, the angular disposition of the CC sites around the chalcogen atoms (Figure 2c, bottom) follows the series  $\text{O} < \text{S} < \text{Se}$  (CC–nucleus–CC = 0, 122.4, 151.2°). Due to the highly diffuse lone pairs of the Te atom in TePA, no (3, −3) CPs of  $L(\mathbf{r})$  are found in its valence shell. They are, however, present in TeMe<sub>2</sub> (CC–nucleus–CC = 157.2°), where the valence shell of the Te atom is activated by the influence of the intramolecular chemical environment (see the Supporting Information). Within the C–Chal–C plane, a couple of CD sites [(3, +1) CP in Figure 2c, top] were found for all four chalcogen atoms with an angular separation  $\text{CD}_1$ –nucleus– $\text{CD}_1$  = 153.1, 152.0, 173.6, and 204.7° for O, S, Se, and Te, respectively. In the case of O and S, the  $\text{CD}_1$  sites belong to a positive area of  $L(\mathbf{r})$  (i.e., the VSCC), while for Se and Te, they belong to a negative one (i.e., the VSCD), showing a larger angular separation. For the S and Se atoms, an additional pair of CD sites was found, and placed closer to the bisector direction ( $\text{CD}_2$ –nucleus– $\text{CD}_2$  = 57.3 and 51.6°, respectively).

Similarly to halogen atoms, the origin of the  $\sigma$ -hole in chalcogens is found in the development of the CD region in the atomic valence shell, the increase of the  $\sigma$ -hole paralleling the extension of the CD region. For O, S, and Se atoms, a third type of CD site [(3, −1) CP] was found along the bisector direction of the C–Chal–C angle ( $\text{CD}_3$ ). At this site,  $\rho(\mathbf{r})$  is at a minimum along the direction linking the maxima of the two CC sites. With dependence on the activation and the molecular environment, either  $\text{CD}_1$ ,  $\text{CD}_2$ , or  $\text{CD}_3$  sites could be involved in the intermolecular interaction.

In a recent combined experimental and theoretical study on Hal...Hal interactions, the electrophilic/nucleophilic power of the CD/CC sites was quantified in a common scale, using the normalized descriptor  $L/\rho$ , where  $L$  and  $\rho$  values were calculated at the critical points of  $L(\mathbf{r})$ .<sup>31</sup> Table 2 shows the  $L/\rho$  values at the CD/CC sites of chalcogen atoms in  $\text{C}_8\text{O}_2\text{H}_4\text{Chal}$  monomers. The electrophilic/nucleophilic power of these sites increases with the more negative/positive magnitudes of  $L/\rho$ . For comparison, the average of  $(L/\rho)_{\text{CD}}$

**Table 2.** Electrophilic and Nucleophilic Power ( $L/\rho$  in  $\text{\AA}^{-2}$ ) of Charge Depletion (CD) and Charge Concentration (CC) Sites in the Electron Valence Shell of the Chalcogen Atoms for the Monomers  $\text{C}_8\text{O}_2\text{H}_4\text{Chal}$  (Chal = O, S, Se, and Te) in Gas Phase

site	O	S	Se	Te
CC	16.89	8.64	−0.09	−
$\text{CD}_1$	8.64	2.19	−6.71	−6.13
$\text{CD}_2$	−	−4.95	−4.26	−
$\text{CD}_3$	−	7.85	−1.65	−

values found for the Cl and Br atoms in  $\text{C}_6\text{Cl}_6$ ,  $\text{C}_6\text{Cl}_5\text{OH}$ ,  $\text{C}_6\text{Br}_6$ , and  $\text{C}_6\text{Br}_5\text{OH}$  monomers (calculated at the same level of theory than  $\text{C}_8\text{O}_2\text{H}_4\text{Chal}$ ) are  $4.35 \pm 0.07$  and  $-5.59 \pm 0.12 \text{ \AA}^{-2}$ , respectively (the statistical dispersion is represented by rms deviation magnitudes). The average of  $(L/\rho)_{\text{CC}}$  values for the same atoms are  $10.95 \pm 0.09$  and  $1.10 \pm 0.13 \text{ \AA}^{-2}$ , respectively.<sup>31</sup> Within the context of the considered molecules, the comparison of the S to Cl atoms and the Se to Br atoms indicates that the electrophilic power of sulfur is more pronounced than that of chlorine (both  $L/\rho_{\text{CD}_1}$  values are lower for the former), while the values of the Se and Br atoms are approximately similar to each other. Accordingly, the nucleophilic power of CC sites decreases along  $\text{O} > \text{S} > \text{Se} > \text{Te}$ , whereas the electrophilic power averaged over the CD sites increases along the same series. In the crystal phase, the  $L/\rho$  magnitudes are expected to be influenced by a redistribution of  $\rho(\mathbf{r})$  due to the interaction of the Chal atom with the molecular environment.

Accurate low-temperature high-resolution X-ray diffraction measurements and ab initio periodic DFT calculations at the experimental geometry with the VASP program<sup>32</sup> have been carried out for SePA to characterize chalcogen bonding. SePA crystallizes in the monoclinic system ( $P2_1/n$  space group,  $Z = 4$ ), with one molecule in the asymmetric unit. The crystalline electron density distribution  $\rho_{\text{cryst}}(\mathbf{r})$  has been fitted against either experimental X-ray or theoretical DFT structure factors by using the multipolar Hansen–Coppens model  $\rho_{\text{mult}}(\mathbf{r})$ .<sup>33</sup> The plot of the experimental deformation  $\Delta\rho(\mathbf{r}) = \rho_{\text{mult}}(\mathbf{r}) - \Sigma\rho_{\text{sph}}^{\text{at}}(\mathbf{r})$  in the intermolecular region around the Se atom suggests chalcogen bonding [ $\text{Se}(\delta^+) \cdots (\delta^-)\text{O}$  and  $[\text{Se}(\delta^-) \cdots (\delta^+)\text{Se}]$  and hydrogen bonding  $[\text{Se}(\delta^-) \cdots (\delta^+)\text{H}]$  interactions (Figure 3a). Very similar results are also observed for the theoretical DFT model (see the Supporting Information).

In the framework of QTAIM,<sup>30a</sup> the topological analysis of  $\rho(\mathbf{r})$  developed by Bader et al. identifies an interatomic interaction by the existence of a bond path between the nuclei, leading to a concomitant bond critical point (bcp), where  $\rho(\mathbf{r})$  exhibits a saddle topology. Figure 3b shows the three intermolecular interactions of the Se atom with its molecular environment. They are identified by the observed bcp's associated to the  $\text{Se} \cdots \text{O}$ ,  $\text{Se} \cdots \text{H}$ , and  $\text{Se} \cdots \text{Se}$  bond paths. The topological and energetic properties of  $\rho(\mathbf{r})$  at bcp's characterize the pairwise interactions. Table 3 gathers the values of the electron density  $\rho$ , the Laplacian  $\nabla^2\rho$ , and the local electron kinetic  $G$  and potential  $V$  energy densities<sup>34</sup> at the bcp's. For the three intermolecular interactions, the values are close to each other and fall into the range determined theoretically and experimentally for weak hydrogen bonds,<sup>34b,35</sup>  $\text{Hal} \cdots \text{Hal}$ ,<sup>31,36</sup> and weak  $\text{Hal} \cdots \text{O}$  (Hal = Cl and Br) interactions.<sup>37</sup> The ratio  $|V|/G < 1$  classifies the three contacts as pure closed-shell interactions of weak intensity,<sup>35b</sup> allowing us to use of the

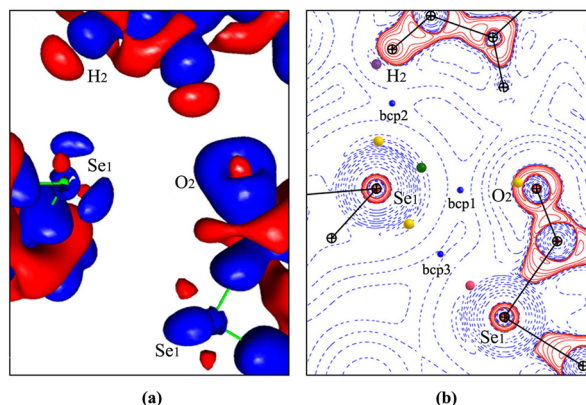


**Figure 3.** Experimental (a)  $\Delta\rho(r)$  (3D) and (b)  $L(r) = -\nabla^2\rho(r)$  maps in the  $\text{Se}^i\text{--O}_2^j\text{--Se}^k$  plane. The  $\Delta\rho(r)$  iso-surfaces (3D) are drawn at the  $\pm 0.05 \text{ e } \text{\AA}^{-3}$  level, positive (blue) and negative (red).  $L(r)$  contours ( $\text{e } \text{\AA}^{-5}$ ) are in logarithmic scale, positive (red) and negative (blue). In (b), intermolecular bond critical points (bcp's) and charge concentration and charge depletion (CC/CD) sites involved in intermolecular interactions with Se are depicted (see Figure 2 for the color descriptions). Symmetry codes: (i)  $x, y, z$ ; (ii)  $1/2 - x, -1/2 + y, 3/2 - z$ ; (iii)  $1/2 + x, 3/2 - y, 1/2 + z$ .

potential energy density for the estimation of the interaction energy ( $E_{\text{int}} \sim -V/2$ ).<sup>31,34b,38</sup> Accordingly, the three interaction energies are small and close to each other ( $E_{\text{int}} \sim 4\text{--}5 \text{ kJ mol}^{-1}$ ), indicating that chalcogen bonding can compete with weak hydrogen bonding in driving molecular packing. The  $E_{\text{int}}$  magnitudes are quite similar to those found in the theoretical calculations (MP2/aug-cc-pVTZ BSSE corrected level of theory) of three  $(\text{SePA})_2$  dimers at the experimental geometries, for which the calculated  $E_{\text{int}}$  and the estimated  $E_{\text{int}} \sim -V/2$  values (in  $\text{kJ mol}^{-1}$ ) are 11.1/9.1 ( $\text{Se}\cdots\text{Se}$  and  $\text{Se}\cdots\text{O}$  interactions in dimer 1), 7.6/5.0 ( $\text{Se}\cdots\text{H}$  interaction in dimer 2), and 19.3/21.3 (two  $\text{O}\cdots\text{H}$  and one  $\text{O}\cdots\text{O}$  interactions in dimer 3). The interaction energy of the corresponding trimer, approximated by the addition of the contributions of the three dimers is 38.0/35.4  $\text{kJ mol}^{-1}$ . As observed in a calculation employing a smaller basis set required for the large trimer size (MP2/6-311++G(d,p), see the Supporting Information), the interaction energy of the trimer (26.3  $\text{kJ mol}^{-1}$ ) is very close to the addition of the interaction energies of the three dimers (5.9, 4.8, and 15.5  $\text{kJ mol}^{-1}$ ), indicating an almost negligible cooperativity.

Compared to the SePA monomer and dimers, the topological analysis of  $L(r)$  in the crystal phase (experimental and theoretical) shows a smaller number of critical points in the valence shell of the Se atom (see the Supporting Information). Indeed, in addition to  $\text{CD}_3$ , only one pair of CD sites is observed between the  $\text{CD}_1$  and  $\text{CD}_2$  sites determined for the isolated monomer (actually,  $\text{CD}_a\text{--nucleus--CD}_b = 152.0^\circ$  and

$154.5^\circ$  for experimental and theoretical models). The angular separation of the CC sites decreases from gas to crystal phases (in the latter,  $\text{CC}_a\text{--nucleus--CC}_b = 118.3^\circ$  and  $119.9^\circ$  for experimental and theoretical models). The directionality of the three intermolecular interactions, which is not obvious from geometrical considerations only, becomes clear from the relative location of the involved CC and CD sites (Figure 3b, Table 3): the angles formed between the  $\text{CD}\cdots\text{CC}$  and internuclear  $\text{Se}\cdots\text{X}$  ( $\text{X} = \text{O}, \text{Se}, \text{and H}$ ) directions are quite small, on average  $12.2 \pm 5.4^\circ$ , whereas the bcp's of  $\rho(r)$ , and therefore the bond paths, are placed nearby the CC–CD line (distances  $0.23 \pm 0.10 \text{ \AA}$ ). A very similar description is found for the theoretical multipolar model. The previous discussions confirm the suggested  $\text{CD}\cdots\text{CC}$  nature of the  $\text{Se}\cdots\text{Se}$ ,  $\text{Se}\cdots\text{O}$ , and  $\text{Se}\cdots\text{H}$  interactions, while the relative location of the involved CC and CD sites can specify their directionality.

Thus, the CD and CC sites face each other in the three intermolecular regions, indicating directional electrophilic–nucleophilic interactions where the Se atom interacts with the molecular environment by involving simultaneously its electrophilic and nucleophilic sites, a situation already observed for halogen atoms.<sup>13,31</sup> In particular, the  $\text{Se}(\text{CC})\cdots(\text{CD})\text{Se}$  interaction can be considered as the analogue of type II homo  $\text{Hal}\cdots\text{Hal}$  interactions, as in solid  $\text{Cl}_2$ ,<sup>39</sup> and  $\text{Hal}_3$  synthons ( $\text{Hal} = \text{Cl}$  and  $\text{Br}$ ).<sup>31</sup> On the other hand, as a consequence of the  $\text{Se}_{\text{CD}}$  and  $\text{O}_{\text{CC}}$  positions (see  $\varphi_1$  and  $\varphi_2$  in Table 3), it is noteworthy that the observed  $\text{C}_1\text{--Se}\cdots\text{O}$  angles ( $i = 1$  and  $2$ ) (Table 1) do not correspond to the distributions centered at  $\zeta_1 \approx 165^\circ$  and  $\zeta_2 \approx 75^\circ$  but to the range  $110\text{--}140^\circ$  in Figure 1b. This feature indicates that the  $L(r)$  function is more appropriate than the  $\sigma$ -hole (approximately along the C–Se bonds) concept to identify electrophilic sites of the Se atoms in  $sp^3$  hybridization.

The electrostatic interaction increases with the electrophilic/nucleophilic power of the charge depletion (CD) and charge concentration (CC) sites, monitored by their  $L/\rho$  values. Accordingly, the quantity  $\Delta(L/\rho) = (L/\rho)_{\text{CC}} - (L/\rho)_{\text{CD}}$  estimates its strength. The experimental and theoretical  $\Delta(L/\rho)$  values in the crystal phase decrease abruptly along the interaction series  $\text{Se}\cdots\text{O}$ ,  $\text{Se}\cdots\text{H}$ , and  $\text{Se}\cdots\text{Se}$  (see Table 4). For the three  $\text{CC}\cdots\text{CD}$  interactions, the significant difference in these values points out the presence of an important energetic contribution that brings closer the  $\text{Se}\cdots\text{Se}$  interaction energy to those of  $\text{Se}\cdots\text{O}$  and  $\text{Se}\cdots\text{H}$  (Table 4). As for halogen atoms,<sup>31</sup> the dispersion component could be invoked to explain this trend,<sup>40</sup> expected to be more significant in the former than in the two latter Se interactions. A close comparative look to the  $\text{Br}\cdots\text{Br}$  interactions in the crystal structures of  $\text{C}_6\text{Br}_6$  and  $\text{C}_6\text{Br}_5\text{OH}$  indicates that the electrophilic/nucleophilic power of CD/CC sites of the Se atom in SePA is less pronounced than those found for the Br atoms [ $-7.7 < (L/\rho)_{\text{CD}} < -4.1 \text{ \AA}^{-2}$  and

**Table 3.** Geometrical Parameters Showing the Directionality of the Charge Concentration $\cdots$ Charge Depletion ( $\text{CC}\cdots\text{CD}$ ) Interactions in the Crystal Phase of SePA<sup>a</sup>

$\text{Se}_{\text{CP}}\cdots\text{X}_{\text{CP}}$	$d_{\text{CC}} (\text{\AA})$	$d_{\text{CD}} (\text{\AA})$	$d_{\text{bcp}} (\text{\AA})$	$\varphi_1 (^\circ)$	$\varphi_2 (^\circ)$	$\alpha (^\circ)$
$\text{Se}^i_{\text{CD}}\cdots\text{O}^j_{\text{CC}}$	0.15/0.18	0.35/0.42	0.34/0.29	112.8/135.8	110.2/119.7	7.7/10.7
$\text{Se}^i_{\text{CC}}\cdots\text{H}^j_{\text{CD}}$	0.20/0.27	0.11/0.16	0.15/0.14	121.3/111.6	112.2/123.2	18.1/7.4
$\text{Se}^i_{\text{CC}}\cdots\text{Se}^j_{\text{CD}}$	0.39/0.41	0.21/0.35	0.21/0.37	108.7/111.5	138.8/127.4	10.7/12.3

<sup>a</sup>For symmetry codes, see Figure 3.  $d_{\text{CC}}/d_{\text{CD}}$  are the distances from the CC/CD sites to the internuclear line between the interacting atoms.  $d_{\text{bcp}}$  is the distance from bcp's of  $\rho(r)$  to the CC–CD direction. Angles  $\varphi_1$  and  $\varphi_2$  are defined as  $\text{C--Se}_{\text{nucleus}}\cdots\text{Se}_{\text{CP}}$  and  $\text{C--Se}_{\text{nucleus}}\cdots\text{X}_{\text{CP}}$ , respectively.  $\alpha$  is the angle between the  $\text{CC}\cdots\text{CD}$  and  $\text{Se}\cdots\text{X}$  directions. Experimental/theoretical magnitudes are left/right values.

Table 4. Characteristics of Intermolecular Se $\cdots$ X (X = O, H, and Se) Interactions in SePA.<sup>a</sup>

Se $\cdots$ X	interaction	<i>d</i>	$\omega$	$\rho$	$\nabla^2\rho$	<i>G</i>	<i>V</i>	<i>V</i> / <i>G</i>	<i>E</i> <sub>int</sub>	$\Delta(L/\rho)$
Se <sup>i</sup> $\cdots$ O <sup>ii</sup>	CD <sub>3</sub> $\cdots$ CC	3.355	98.1	0.049/0.049	0.62/0.62	13.3/13.3	−9.7/−9.7	0.73/0.73	4.9/4.9	20.4/22.1
Se <sup>i</sup> $\cdots$ H <sup>iii</sup>	CC <sub>a</sub> $\cdots$ CD	2.974	95.9	0.050/0.052	0.51/0.50	11.5/11.4	−8.9/−9.1	0.77/0.80	4.5/4.6	14.8/11.4
Se <sup>i</sup> $\cdots$ Se <sup>ii</sup>	CC <sub>b</sub> $\cdots$ CD	3.822	100.6	0.051/0.047	0.37/0.37	9.0/8.6	−7.8/−7.2	0.87/0.84	3.9/3.6	2.5/3.1

<sup>a</sup>For symmetry codes, see Figure 3. Distance (*d*/Å), penetration parameter ( $\omega$ /%), topological ( $\rho$ /e Å<sup>−3</sup>,  $\nabla^2\rho$ /e Å<sup>−5</sup>), and energetic (*G*, *V*/kJ mol<sup>−1</sup> bohr<sup>−3</sup>) properties are calculated at the bcp's of  $\rho(\mathbf{r})$ . The  $\Delta(L/\rho)$ /Å<sup>−2</sup> parameter is calculated as  $\Delta(L/\rho) = (L/\rho)_{CC} - (L/\rho)_{CD}$ . The interaction energy (kJ mol<sup>−1</sup>) is estimated from  $E_{int} \sim -V/2$ . Experimental/theoretical magnitudes are left/right values.

0.5 < (*L*/ $\rho$ )<sub>CC</sub> < 4.1 Å<sup>−2</sup>].<sup>31</sup> As measured from  $\Delta(L/\rho)$ , the resulting electrostatic interaction is greater for Br $\cdots$ Br [ $\Delta(L/\rho) = 6.8 \pm 2.6$  Å<sup>−2</sup>] than for Se $\cdots$ Se (Table 3). Along with the electrostatic descriptor  $\Delta(L/\rho)$ , the estimated interaction energy *E*<sub>int</sub> for Se $\cdots$ Se is also lower in magnitude than that of Br $\cdots$ Br (<*E*<sub>int</sub>> = 5.1 ± 1.2 kJ mol<sup>−1</sup> with <*d*<sub>Br $\cdots$ Br</sub>> = 3.62 ± 0.11 Å).<sup>31</sup>

In summary, directionality is one of the most important characteristics of chalcogen bonding. It is controlled by dominantly electrostatic electrophilic–nucleophilic interactions, which are established by placing face-to-face CD $\cdots$ CC regions and are quantitatively monitored by  $\Delta(L/\rho) = (L/\rho)_{CC} - (L/\rho)_{CD}$  magnitudes. As a consequence of the charge density polarization in the chemical bond and the *sp*<sup>3</sup> hybridization of the chalcogen atom, CD/ $\delta^+$  regions are observed approximately along the C–Chal directions and give rise to two  $\sigma$ -holes, while CC/ $\delta^-$  regions are in the perpendicular plane bisecting the C–Chal–C group due to the location of the lone pairs. The concerted increase/decrease of the extension of CD/CC regions along the series O < S < Se < Te follows the progressive depletion of  $\rho(\mathbf{r})$  in the chalcogen valence shell. In this process, topological CD sites dominate a progressively enlarged electrophilic region within the C–Chal–C plane, while two nucleophilic regions significantly separate and weaken in a perpendicular disposition to the former. Chalcogen and halogen bonding exhibit many similarities because the electronic driving force is the interaction of atomic CD/ $\delta^+$  and CC/ $\delta^-$  regions. Thus, both are highly directional and increase in strength with the atom size. From the results of this study, the series Chal = O, S, Se, and Te could be put in front of Hal = F, Cl, Br, and I to expect roughly similar interaction energies when comparing chalcogen (Chal $\cdots$ X) to halogen (Hal $\cdots$ X) bonding interactions at similar penetrations (Chal and Hal by pairs of closest atoms). However, as the dispersion component is expected to be slightly larger in halogen than in chalcogen bonding, interaction energies are expected to be somewhat larger for the former. Main differences between chalcogen and halogen bonding can be attributed to the particular orientation of CD and CC regions in chalcogen and halogen atoms, leading to specific directionalities in their electrophilic–nucleophilic interactions. This important trend indicates that chalcogen and halogen bonding can drive different geometrical preferences of molecular packing and therefore they can be put in perspective to design specific molecular arrangements in supramolecular chemistry and crystal engineering.

## ■ ASSOCIATED CONTENT

### Supporting Information

Experimental details on data collection and multipolar refinement along with the multipolar parameters and residual electron density maps of selenophthalic anhydride (SePA), gas-phase and periodic theoretical calculations details, and

geometrical parameters showing the directionality of the CC $\cdots$ CD interactions in the crystal phase of SePA. This material is available free of charge via the Internet at <http://pubs.acs.org>.

## ■ AUTHOR INFORMATION

### Corresponding Author

\*E-mail: [enrique.espinosa@crm2.uhp-nancy.fr](mailto:enrique.espinosa@crm2.uhp-nancy.fr).

### Notes

The authors declare no competing financial interest.

## ■ ACKNOWLEDGMENTS

This work has been supported by the French “Agence Nationale de la Recherche” (Grant ANR-08-BLAN-0091-01). M.E.B. thanks the French ANR for a Ph.D. fellowship from the same grant. The “Service Commun de Diffraction X” of Université de Lorraine is thanked for providing access to crystallographic facilities. GENCI-CINES (Grant 2012-X2012085106) is thanked for providing access to computing facilities.

## ■ REFERENCES

- (1) Lehn, J.-M. *Angew. Chem.* **1988**, *100*, 91–116; *Angew. Chem., Int. Ed.* **1988**, *27*, 89–112.
- (2) (a) Jeffrey, G. A.; Saenger, W. *Hydrogen Bonding in Biological Structures*; Springer: Berlin, 1991. (b) Steiner, T. *Angew. Chem.* **2002**, *114*, 51–80; *Angew. Chem., Int. Ed.* **2002**, *41*, 48–76.
- (3) (a) Desiraju, G. R.; Steiner, T. *The Weak Hydrogen Bond*; Oxford University Press: New York, 1991. (b) Steiner, T. *New J. Chem.* **1998**, 1099–1103.
- (4) Nishio, M.; Hirota, M.; Umezawa, Y. *The CH/ $\pi$  Interaction*; Wiley-VCH: New York, 1998.
- (5) Metrangolo, P.; Resnati, G. *Halogen Bonding: Fundamentals and Applications*; Springer: Berlin, 2008.
- (6) Guthrie, F. J. *Chem. Soc.* **1863**, *16*, 239–244.
- (7) Vonnegut, B.; Warren, B. E. *J. Am. Chem. Soc.* **1936**, *58*, 2459–2461.
- (8) Hassel, O. *Science* **1970**, *170*, 497–502.
- (9) Bent, H. A. *Chem. Rev.* **1968**, *68*, 587–648.
- (10) (a) Politzer, P.; Lane, P.; Concha, M. C.; Ma, Y.; Murray, J. S. *J. Mol. Model.* **2007**, *13*, 305–311. (b) Politzer, P.; Murray, J. S.; Lane, P. *Int. J. Quantum Chem.* **2007**, *107*, 3046–3052. (c) Awwadi, F. F.; Willett, R. D.; Peterson, K. A.; Twamley, B. *Chem.—Eur. J.* **2006**, *12*, 8952–8960.
- (11) Tsuzuki, S.; Wakisaka, A.; Ono, T.; Sonoda, T. *Chem.—Eur. J.* **2012**, *18*, 951–960.
- (12) (a) Metrangolo, P.; Neukirch, H.; Pilati, T.; Resnati, G. *Acc. Chem. Res.* **2005**, *38*, 386–395. (b) Fourmigué, M.; Batail, P. *Chem. Rev.* **2004**, *104*, 5379–5418.
- (13) (a) Bui, T. T. T.; Dahanoui, S.; Lecomte, C.; Desiraju, G. R.; Espinosa, E. *Angew. Chem., Int. Ed.* **2009**, *48*, 3838–3841. (b) Aubert, E.; Lebègue, S.; Marsman, M.; Bui, T. T. T.; Jelsch, C.; Dahanoui, S.; Espinosa, E.; Ángyán, J. G. *J. Phys. Chem. A* **2011**, *115*, 14484–14494.
- (14) Stone, A. J. *J. Am. Chem. Soc.* **2013**, *135*, 7005–7009.
- (15) (a) Iwaoaka, M.; Takemoto, S.; Tomoda, S. *J. Am. Chem. Soc.* **2002**, *124*, 10613–10620. (b) Réthoré, C.; Madalan, A.; Fourmigué,



- M.; Canadell, E.; Lopes, E.; Almeida, M.; Clérac, R.; Avarvari, N. *New J. Chem.* **2007**, *31*, 1468–1483.
- (16) Rosenfield, R. E., Jr.; Parthasarathy, R.; Dunitz, J. D. *J. Am. Chem. Soc.* **1977**, *99*, 4860–4862.
- (17) Guru Row, T. N.; Parthasarathy, R. *J. Am. Chem. Soc.* **1981**, *103*, 477–479.
- (18) (a) Bleiholder, C.; Werz, D. B.; Köppel, H.; Gleiter, R. *J. Am. Chem. Soc.* **2006**, *128*, 2666–2674. (b) Bleiholder, C.; Gleiter, R.; Werz, D. B.; Köppel, H. *Inorg. Chem.* **2007**, *46*, 2249–2260.
- (19) (a) Wang, W.; Ji, B.; Zhang, Y. *J. Phys. Chem. A* **2009**, *113*, 8132–8135. (b) Sánchez-Sanz, G.; Trujillo, C.; Alkorta, I.; Elguero, J. *ChemPhysChem* **2012**, *13*, 496–503.
- (20) (a) Li, Q.-Z.; Li, R.; Guo, P.; Li, H.; Li, W.-Z.; Cheng, J.-B. *Comput. Theor. Chem.* **2012**, *980*, 56–61. (b) Bleiholder, C.; Werz, D. B.; Köppl, H.; Gleiter, R. *J. Am. Chem. Soc.* **2006**, *128*, 2666–2674. (c) Bleiholder, C.; Gleiter, R.; Werz, D. B.; Köppl, H. *Inorg. Chem.* **2007**, *46*, 2249–2260.
- (21) (a) Iwaoka, M.; Komatsu, H.; Katsuda, T.; Tomoda, S. *J. Am. Chem. Soc.* **2002**, *124*, 1902–1909. (b) Cozzolino, A. F.; Vargas-Baca, I.; Mansour, S.; Mahmoudkhani, A. H. *J. Am. Chem. Soc.* **2005**, *127*, 3184–3190.
- (22) (a) Dahaoui, S.; Pichon-Pesme, V.; Howard, J. A. K.; Lecomte, C. *J. Phys. Chem. A* **1999**, *103*, 6240–6250. (b) Scherer, W.; Spiegler, M.; Pedersen, B.; Tafipolsky, M.; Hieringer, W.; Reinhard, B.; Downs, A.; McGrady, G. S. *Chem. Commun. (Cambridge, U.K.)* **2000**, 635–636. (c) Lee, C.-R.; Tang, T.-H.; Chen, L.; Wang, C.-C.; Wang, Y. *J. Phys. Chem. Solids* **2004**, *65*, 1957–1966.
- (23) Bondi, A. *J. Phys. Chem.* **1964**, *68*, 441–451.
- (24) Bresciani, N.; Calligaris, M. *Acta Crystallogr., Sect. B* **1975**, *31*, 2685–2686.
- (25) Majeed, Z.; McWhinnie, W. R.; Paxton, K.; Hamor, T. A. *J. Organomet. Chem.* **1999**, *577*, 15–18.
- (26) Allen, F. H. *Acta Crystallogr., Sect. B* **2002**, *58*, 380–388.
- (27) Koketsu, M.; Nada, F.; Hiramatsu, S.; Ishihara, H. *J. Chem. Soc., Perkin Trans. 1* **2002**, 737–740.
- (28) (a) Kresse, G.; Hafner, J. *Phys. Rev. B* **1993**, *47*, 558–561. (b) Kresse, G.; Hafner, J. *J. Phys.: Condens. Matter* **1994**, *6*, 8245–8257. (c) Kresse, G.; Furthmüller, J. *Comput. Mater. Sci.* **1996**, *6*, 15–50. (d) Kresse, G.; Furthmüller, J. *Phys. Rev. B* **1996**, *54*, 11169–11186.
- (29) Perdew, J. P.; Burke, K.; Ernzerhof, M. *J. Chem. Phys.* **1996**, *77*, 3865–3868.
- (30) (a) Bader, R. F. W. *Atoms in Molecules – A Quantum Theory*; Clarendon: Oxford, 1990. (b) Bader, R. F. W. *J. Phys. Chem. A* **1998**, *102*, 7314–7323. (c) Bader, R. F. W. *J. Phys. Chem. A* **2009**, *113*, 10391–10396.
- (31) Brezgunova, M. E.; Aubert, E.; Dahaoui, S.; Fertey, P.; Lebègue, S.; Jelsch, C.; Ángyán, J. A.; Espinosa, E. *Cryst. Growth Des.* **2012**, *12*, 5373–5386.
- (32) (a) Kresse, G.; Hafner, J. *Phys. Rev. B* **1993**, *47*, 558–561. (b) Kresse, G.; Hafner, J. *J. Phys.: Condens. Matter* **1994**, *6*, 8245–8257. (c) Kresse, G.; Furthmüller, J. *Comput. Mater. Sci.* **1996**, *6*, 15–50. (d) Kresse, G.; Furthmüller, J. *Phys. Rev. B* **1996**, *54*, 11169–11186.
- (33) Hansen, N. K.; Coppens, P. *Acta Crystallogr., Sect. A* **1978**, *34*, 909–921.
- (34) (a) Abramov, Yu. A. *Acta Crystallogr., Sect. A* **1997**, *53*, 264–272. (b) Espinosa, E.; Molins, E.; Lecomte, C. *Chem. Phys. Lett.* **1998**, *285*, 170–173. (c) Espinosa, E.; Alkorta, I.; Rozas, I.; Elguero, J.; Molins, E. *Chem. Phys. Lett.* **2001**, *336*, 457–461.
- (35) (a) Espinosa, E.; Souhassou, M.; Lachekar, H.; Lecomte, C. *Acta Crystallogr., Sect. B* **1999**, *55*, 563–572. (b) Espinosa, E.; Alkorta, I.; Elguero, J.; Molins, E. *J. Chem. Phys.* **2002**, *117*, 5529–5542. (c) Mata, I.; Alkorta, I.; Molins, E.; Espinosa, E. *Chem.—Eur. J.* **2010**, *16*, 2442–2452.
- (36) Hathwar, V. R.; Guru Row, T. N. *J. Phys. Chem. A* **2010**, *114*, 13434–13441.
- (37) (a) Hathwar, V. R.; Gonnade, R. G.; Munchi, P.; Bhadbhade, M. M.; Guru Row, T. N. *Cryst. Growth Des.* **2011**, *11*, 1855–1862.
- (b) Bach, A.; Lentz, D.; Luger, P. *J. Phys. Chem. A* **2001**, *105*, 7405–7412. (c) Bianchi, R.; Forni, A.; Pilati, T. *Acta Crystallogr., Sect. B* **2004**, *60*, 559–568.
- (38) Dominiak, P. M.; Espinosa, E.; Ángyán, J. G. In *Modern Charge Density Analysis*; Gatti, C.; Macchi, P., Eds.; Springer: Berlin, 2012; 387–434.
- (39) Tsirelson, V. G.; Zou, P. F.; Tang, T. H.; Bader, R. F. W. *Acta Crystallogr., Sect. A* **1995**, *51*, 143–153.
- (40) Sánchez-Sanz, G.; Trujillo, C.; Alkorta, I.; Elguero, J. *ChemPhysChem* **2012**, *13*, 496–503.